

The Heavy Photon Search Test Detector

M. Battaglieri^a, S. Boyarinov^b, S. Buelmann^c, V. Burkert^b, G. Charles^d, W. Cooper^e, N. Dashyan^f, R. De Vita^a, A. Deur^b, R. Dupre^d, H. Egiyan^b, L. Elouadrhiri^b, R. Essig^g, V. Fadeyev^h, C. Fieldⁱ, A. Freyberger^b, N. Gevorgyan^f, F.-X. Girod^b, N. Grafⁱ, M. Grahamⁱ, K. Griffioen^j, A. Grillo^h, M. Guidal^d, G. Hallerⁱ, P. Hansson Adrian^{i,*}, R. Herbstⁱ, M. Holtrop^k, J. Jarosⁱ, S. K. Phillips^k, M. Khandaker^l, A. Kubarovskiy^m, T. Maruyamaⁱ, J. McCormickⁱ, K. Moffeitⁱ, O. Moreno^h, H. Nealⁱ, T. Nelsonⁱ, S. Niccolai^d, A. Odianⁱ, M. Oriunnoⁱ, R. Paremuzyan^f, E. Rauly^d, E. Rindel^d, P. Rosier^d, C. Salgado^l, P. Schusterⁿ, Y. Sharabian^b, K. Slifer^k, D. Sokhan^o, S. Stepanyan^b, P. Stoler^m, N. Toroⁿ, S. Uemuraⁱ, M. Ungaro^b, H. Voskanyan^f, D. Walzⁱ, L. Weinstein^c, B. Wojtsekhowski^b

^a*Istituto Nazionale di Fisica Nucleare, Sezione di Genova e Dipartimento di Fisica dell'Università, 16146 Genova, Italy*

^b*Thomas Jefferson National Accelerator Facility, Newport News, Virginia 23606*

^c*Old Dominion University, Norfolk, Virginia 23529*

^d*Institut de Physique Nucléaire d'Orsay, IN2P3, BP 1, 91406 Orsay, France*

^e*Fermi National Accelerator Laboratory, Batavia, IL 60510-5011*

^f*Yerevan Physics Institute, 375036 Yerevan, Armenia*

^g*Stony Brook University, Stony Brook, NY 11794-3800*

^h*University of California, Santa Cruz, CA 95064*

ⁱ*SLAC National Accelerator Laboratory, Menlo Park, CA 94025*

^j*The College of William and Mary, Department of Physics, Williamsburg, VA 23185*

^k*University of New Hampshire, Department of Physics, Durham, NH 03824*

^l*Norfolk State University, Norfolk, Virginia 23504*

^m*Rensselaer Polytechnic Institute, Department of Physics, Troy, NY 12181*

ⁿ*Perimeter Institute, Ontario, Canada N2L 2Y5*

^o*University of Glasgow, Glasgow, G12 8QQ, Scotland, UK*

Abstract

The Heavy Photon Search (HPS), an experiment to search for a hidden sector photon in fixed target electroproduction, is preparing for installation at the Thomas Jefferson National Accelerator Facility (JLab) in the Fall of 2014. As the first stage of this project, the HPS Test Run apparatus was constructed and operated in 2012 to demonstrate the experiment's technical feasibility and to confirm that the trigger rates and occupancies are as expected. This paper describes the HPS Test Run apparatus and readout electronics and its performance. In this setting, a heavy photon can be identified as a narrow e^+e^- mass peak above the trident background or as a decay vertex displaced from the production target, so charged particle tracking and vertexing are needed for its detection. In the HPS Test Run, charged particles are measured with a compact forward silicon microstrip tracker inside a dipole magnet. Electromagnetic showers are detected in a PbWO₄ crystal calorimeter situated behind the magnet used to trigger the experiment and identify electrons and positrons. Both detectors are placed close to the beam line and split top-bottom. This arrangement provides sensitivity to low-mass heavy photons, allows clear passage of the unscattered beam, and avoids the spray of degraded electrons coming from the target. The discrimination between prompt and displaced e^+e^- pairs requires the first layer of silicon sensors be placed only 10 cm downstream of the target. The expected signal is small, and the trident background huge, so the experiment requires very large statistics. Accordingly, the HPS Test Run utilizes high-rate readout and data acquisition electronics and a fast trigger to perfectly exploit the essentially 100% duty cycle of the CEBAF accelerator.

Keywords: silicon microstrip, tracking, vertexing, heavy photon, dark photon, hidden sector, electromagnetic calorimeter

*Corresponding author.

Email address: phansson@slac.stanford.edu (P. Hansson Adrian)

1 **Contents**

2	1	Introduction	3
3	2	Detector Overview	3
4	3	The HPS Test Run Beamline	5
5	4	Silicon Vertex Tracker	5
6	4.1	Layout	6
7	4.2	Components	7
8	4.3	Production, Assembly and Shipping . .	7
9	4.4	Alignment	8
10	5	Electromagnetic Calorimeter	8
11	5.1	Components	8
12	5.2	Layout	8
13	5.3	Signal readout	9
14	6	Trigger and Data Acquisition	9
15	6.1	Trigger system	9
16	6.2	SVT Data Acquisition	9
17	6.3	General Data Acquisition and Online Computing	10
19	7	Reconstruction and Performance	10
20	7.1	SVT Performance	10
21	7.1.1	Cluster and Hit Reconstruction .	11
22	7.1.2	Momentum and Vertexing Res- olution	12
23	7.2	ECal Performance	12
24	7.3	Trigger Performance	13
25	7.4	Trigger Rate Comparisons	14
27	8	Summary and Outlook	14
28	9	Acknowledgements	15

29 **1. Introduction**

30 The heavy photon (A'), aka a "hidden sector" or
31 "dark" photon, is a particle with mass $10 - 1000$ MeV
32 which couples weakly to electric charge by mixing with
33 the Standard Model photon [1]. Consequently, it can
34 be radiated by electrons and subsequently decay into
35 e^+e^- pairs, albeit at rates far below those of QED tri-
36 dent processes. Heavy photons have been suggested by
37 numerous beyond Standard Model theories [2], to ex-
38 plain the discrepancy between theory and experiment of
39 the muon's $g - 2$ [3], and as a possible explanation of
40 recent astrophysical anomalies. Heavy photons couple
41 directly to hidden sector particles with "dark" or "hid-
42 den sector" charge; these particles could constitute all
43 or some of the dark matter [4]. Current phenomenology
44 highlights the $20 - 1000$ MeV/c 2 mass range, and sug-
45 gests that the coupling to electric charge, ϵe , has ϵ in the
46 range of $10^{-3} - 10^{-5}$. This range of parameters makes
47 A' searches viable in medium energy fixed target elec-
48 troproduction [5], but requires large data sets and good
49 mass resolution to identify a small mass peak above the
50 copious QED background. At small couplings, A' be-
51 come long-lived, so detection of a displaced decay ver-
52 tex can reject the prompt QED background and boost
53 experimental sensitivity.

54 The HPS experiment [6] uses both invariant mass and
55 secondary vertex signatures to search for A' . It uses a
56 ≈ 1 m long silicon tracking and vertexing detector in-
57 side a dipole magnet to measure charged particle trajec-
58 tories and a fast electromagnetic calorimeter just down-
59 stream of the magnet to provide a trigger and identify
60 electrons. The experiment utilizes very high rate front
61 end electronics and runs at high trigger rates (up to
62 50kHz), exploiting the 100% duty cycle of the Thomas
63 Jefferson National Accelerator Facility (JLab) CEBAF
64 accelerator to accumulate the needed statistics.

65 The HPS Test Run apparatus, a simplified version
66 of the HPS experiment, was proposed and approved at
67 JLab as the first stage of HPS. Its purposes included
68 demonstrating that the apparatus and data acquisition
69 systems are technically feasible and the trigger rates and
70 occupancies to be encountered in electron-beam run-
71 ning are as simulated. Given dedicated running time
72 with electron beams, the HPS Test Run apparatus is ca-
73 pable of searching for heavy photons in unexplored re-
74 gions of parameter space. The key design criteria for
75 HPS and the HPS Test Run are the same:

- 76 • large and uniform acceptance in the forward region
77 close to the beam in order to catch boosted A' de-
78 cay products,

- 79 • beam passage through the apparatus in vacuum, to
80 eliminate direct interactions with the detector and
81 minimize beam gas interactions,
- 82 • a flexible, redundant and efficient trigger selecting
83 electron and positron pairs at rates up to 50 kHz,
- 84 • excellent track reconstruction efficiency for elec-
85 trons and positrons,
- 86 • good angular and momentum resolution to recon-
87 struct invariant mass precisely,
- 88 • excellent vertex resolution to discriminate dis-
89 placed A' decays from prompt QED backgrounds,
- 90 • high rate electronics with excellent timing resolu-
91 tion to minimize out of time backgrounds,
- 92 • data handling rates of 100 MB/s to permanent stor-
93 age,
- 94 • detector components that can survive and effi-
95 ciently operate in a high radiation environment
96 with local doses exceeding 100 Mrad.

97 The HPS Test Run apparatus was installed on April
98 19, 2012, and ran parasitically in the photon beam of
99 the HDice experiment [7] until May 18. The JLab run
100 schedule precluded any dedicated electron beam run-
101 ning, but the HPS Test Run was allowed a short and
102 valuable dedicated run at the end of scheduled CE-
103 BAF running. This final running provided enough data
104 to demonstrate the functionality of the apparatus, doc-
105 ument its performance, and explore trigger rates, as
106 shown below. This paper reviews the HPS Test Run ap-
107 paratus; documents the performance of the trigger, data
108 acquisition, silicon tracking detector, and the electro-
109 magnetic calorimeter at the level assumed in calculating
110 the physics reach of the HPS experiment.

111 This paper reviews the HPS Test Run apparatus;
112 documents the performance of the trigger, data acqui-
113 sition, silicon tracking detector, and the electro-
114 magnetic calorimeter at the level assumed in calculating the
115 physics reach of the HPS experiment.

116 **2. Detector Overview**

117 The HPS Test Run apparatus was designed to run
118 in Hall B at JLab using the CEBAF electron beam, a
119 499 MHz beam, at energies of 2.2 and 6.6 GeV and cur-
120 rents between 200 and 600 nA. The overall design of
121 the experiment follows from the kinematics of A' pro-
122 duction which typically results in a final state particle

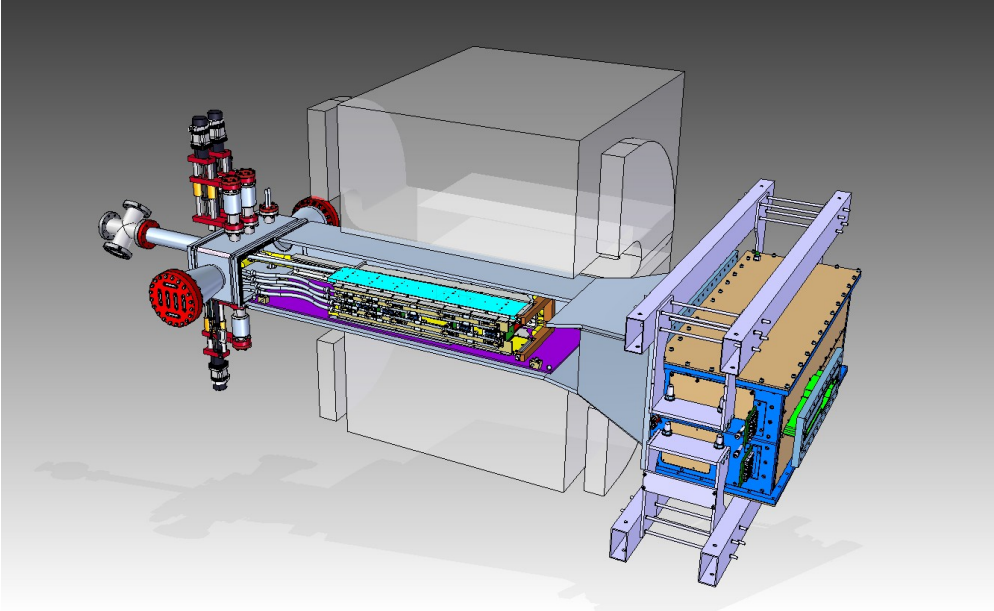


Figure 1: Rendering of the HPS Test Run apparatus installed on the beam line.

123 within a few degrees of the incoming beam, especially 150
 124 at low $m_{A'}$. Detectors must therefore be placed close 151
 125 to the beam. The intense electron beam enlarges down- 152
 126 stream after multiple scattering in the target and elec- 153
 127 trons which have radiated in the target disperse horizon- 154
 128 tally in the field of the analyzing magnet. Together they 155
 129 constitute a "wall of flame" which must be completely 156
 130 avoided. Accordingly, the apparatus is split vertically 157
 131 to avoid a "dead zone", the region within ± 15 mrad of 158
 132 the beam plane. In addition, the beam is transported in 159
 133 vacuum through the tracker to minimize beam-gas inter- 160
 134 action backgrounds. Even with these precautions, the 161
 135 occupancies of sensors near the beam plane are high, 162
 136 dominated by the multiple Coulomb scattering of the 163
 137 primary beam, so high rate detectors, a fast trigger, and 164
 138 excellent time tagging are required to minimize their 165
 139 impact. The trigger comes from a highly-segmented 166
 140 lead-tungstate (PbWO_4) crystal calorimeter located just 167
 141 downstream of the dipole magnet.
 142

143 A rendering of the apparatus installed on the beam line 171
 144 is shown in Fig. 1 and an overview of the coverage, seg- 172
 145 mentation and performance is given in Tab. 1.

146 The silicon vertex tracking and vertexing detector for 173
 147 HPS Test Run, or SVT, resides in a vacuum chamber in- 174
 148 side the Pair Spectrometer (PS) dipole magnet in Hall 175
 149 B at JLab. The SVT has five measurement stations,
 176
 177

or "layers," beginning 10 cm downstream of the target. 150
 Each layer comprises a pair of closely-spaced silicon 151
 microstrip sensors responsible for measuring a single 152
 coordinate, or "view". Introduction of a small (50 or 153
 100 mrad) stereo angle between the two sensors of each 154
 layer provides three-dimensional tracking and vertexing 155
 throughout the acceptance of the detector. In order to 156
 accommodate the dead zone, the SVT is built in two 157
 halves that are approximately mirror reflections of one 158
 another about the plane of the nominal electron beam. 159
 Each layer in one half is supported on a common sup- 160
 port plate with independent cooling and readout.
 161

162 The electromagnetic calorimeter (ECal) is also split 163 into two halves. Each half of the ECal consists of 164
 221 PbWO_4 crystals arranged in rectangular formation. 165
 There are five rows with 46 modules in each row except 166
 the row closest to the beam plane which has 37. The 167
 light from each crystal is read out by an Avalanche 168
 Photodiode (APD) glued on the back surface of the 169
 crystal. Signals from the APDs are amplified using custom- 170
 made amplifier boards before being sent to the data ac- 171
 quisition electronics.

172 The Data Acquisition system combines two architec- 173
 tures, the Advanced Telecom Communications Archi- 174
 tecture (ATCA) based SVT readout system and VME- 175
 bus Switched Serial (VXS) based digitization and trig- 176
 gering system for the ECal. The system was designed 177
 to run at up to 20 kHz trigger rate.

Table 1: Overview of the coverage, segmentation and performance of the HPS Test Run detector.

System	Coverage (mrad)	# channels	ADC (bit)	Time resolution (ns)	# layers	Segmentation	Performance
SVT	$15 < \theta_y < XXXX$	12800	14	≈ 2 ns	5 (stereo layers)	$\approx 120 \mu\text{m} r - \phi$ $\approx 6 \mu\text{m} z$	$\sigma_{d0,y} \approx 100 \mu\text{m}$ $\sigma_{d0,x} \approx 300 \mu\text{m}$ $\sigma_{d0,z} \approx 1 \text{ mm}$
Ecal	$15 < \theta_y < XXXX$	442	12	4 ns	1	$1.33 \times 1.33 \text{ cm}^2$ $1.6 \times 1.6 \text{ cm}^2$	$\sigma(E)/E \approx 4.5\%$

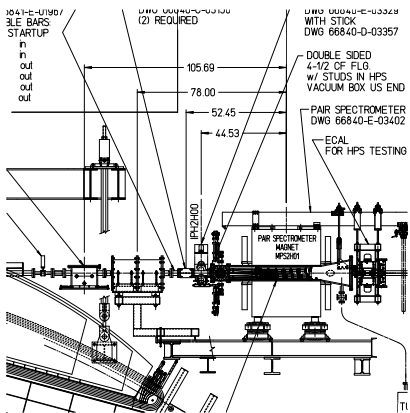


Figure 2: Layout of the HPS parasitic run.

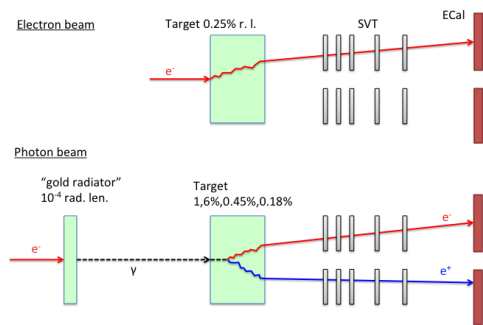


Figure 3: Illustrative comparison of HPS Test Run photon beam compared to the HPS electron beam.

178 3. The HPS Test Run Beamline

179 The HPS Test Run studied multiple Coulomb scattering of electrons and positrons from bremsstrahlung photons produced in the Hall B tagged photon facility. 180 Figure 2 shows the layout of the setup on the beam line. 181 The SVT was installed inside the Hall B pair spectrometer magnet vacuum chamber with the ECal mounted downstream of it. Both the SVT and the ECal were retracted off the beam plane compared to nominal electron beam running to allow clean passage of the photon beam through the system.

182 The photon beam was generated in the interaction of 183 5.5 GeV electrons with a $10^{-4} X_0$ gold radiator located 184 ≈ 9 m upstream of the PS. The primary beam and scattered 185 electrons are deflected away from detectors by the 186 dipole magnet of the photon tagging system. During the 187 dedicated HPS Test Run period, the collimated (6.4 mm 188 diameter), photon beam passes through the PS pair converter 189 gold foil and later the HPS system as illustrated in Fig. 3. 190 The PS pair converter was located ≈ 77 cm upstream of the first layer of the SVT.

191 Data was taken on three different converter thicknesses 192 with photon fluxes between $0.4\text{-}1.3 \times 10^8/\text{s}$ 193 ($0.55 < E_\gamma < 5.5$ GeV) at beam currents varying 194 between 30-90 nA and repeated with the reverse field set- 195 196 197 198 199 200 201 202

Converter thickn. (% X_0)	Duration (s)	e^- on radiator (μC)
1.6	911	24.4
0.18	2640	193.5
0.45	2149	140.7
0	1279	88.1

Table 2: Measured integrated currents for the dedicated photon runs.

203 ting of the PS dipole magnet. The photon beam line 204 during the HPS Test Run produced a relatively large 205 fraction of pairs originating upstream of the converter 206 position. This contribution was measured during data 207 taking with “empty” converter runs i.e. removing the 208 converter but with all other conditions the same. The 209 runs taken during the time dedicated to HPS Test Run is 210 summarized in Tab. 2.

211 4. Silicon Vertex Tracker

The Silicon Vertex Tracker (SVT) enables efficient reconstruction of charged particles and precision determination of their trajectories. These measurements allow A' decays to be distinguished from background via simultaneous estimation of the invariant mass of e^+e^-

217 decay products and the position of decay vertexes downstream of the target.
218

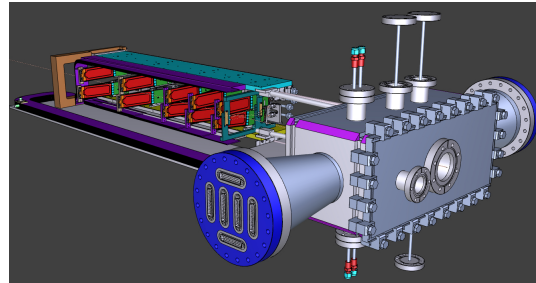
219 The design of the SVT is primarily driven by direct
220 physics requirements and constraints from the environment
221 at the interaction region. The A' decay products
222 have momenta in the range of 1 GeV, so multiple scattering
223 dominates mass and vertexing uncertainties for
224 any possible material budget, so the SVT must minimize
225 the amount of material in the tracking volume.
226 The signal yield for long-lived A' is very small, so the
227 rejection of prompt vertexes must be exceedingly pure,
228 on the order of 10^{-7} , in order to eliminate all prompt
229 backgrounds. To achieve the required vertexing performance
230 the first layer of the SVT must be placed no more than about 10 cm downstream of the target.
231 At that distance, it is found that the active region of
232 a sensor can be placed as close to 1.5 mm from the center of the beam, defining the 15 mrad “dead zone”
233 mentioned previously, to maximize low-mass A' acceptance
234 with decay products nearly collinear with the beam axis. At the edge of this “dead zone,” the radiation
235 dose approaches 10^{15} electrons/cm²/month, or roughly
236 3×10^{14} 1 MeV neutron equivalent/cm²/month [8], requiring
237 the sensors to be actively cooled. Meanwhile,
238 very low-energy delta rays from beam-gas interactions
239 multiply the density of background hits, so the SVT
240 must operate inside the beam vacuum. Finally, in order
241 to protect the sensors, the detector must be movable
242 so that it can be retracted during periods of uncertain
243 beam conditions.

247 4.1. Layout

248 The layout of the SVT is summarized in Tab. 4.1 and
249 rendered in Fig. 4. Each of the layers is comprised
250 of a pair of closely-spaced silicon microstrip sensors
251 mounted back-to-back to form a module. A 100 mrad
252 stereo angle is used in the first three layers to provide
253 higher-resolution 3D space points for vertexing. Using
254 50 mrad in the last two layers breaks the tracking
255 degeneracy of having five identical layers and minimizes
256 fakes from ghost hits to improve pattern recognition.
257 Altogether, the SVT has 20 sensors for a total of 12780
258 readout channels.

Layer	1	2	3	4	5
<i>z</i> from target (cm)	10	20	30	50	70
Stereo angle (mrad)	100	100	100	50	50
Bend res. (μm)	≈ 60	≈ 60	≈ 60	≈ 120	≈ 120
Non-bend res. (μm)	≈ 6	≈ 6	≈ 6	≈ 6	≈ 6
# of sensors	4	4	4	4	4
Dead zone (mm)	± 1.5	± 3.0	± 4.5	± 7.5	± 10.5
Power cons. (W)	6.9	6.9	6.9	6.9	6.9

259 Table 3: Layout of the SVT.



260 Figure 4: A rendering of the SVT showing the modules on their support plates held by the hinged C-support on the left and the motion levers on the right. The sensors are shown in red and the hybrid readout boards in green. The beam enters from the right through a vacuum box with flanges for services.

261 The SVT is built in two separate halves that are mirror
262 reflections of one another about the plane of the nominal
263 electron beam. Each half consists of five modules
264 mounted on a support plate that provides services to the
265 modules and allows them to be moved as a group relative
266 to the dead zone. The two halves of the tracker are connected
267 to hinges mounted on a C-shaped support just beyond the last layer that defines the nominal spacing
268 between the upper and lower halves of the tracker. A shaft attached to each support plate in front of layer
269 1 extends upstream and connects to a linear shift that
270 transfers motion into the vacuum box through bellows
271 to open and close the two halves around the dead zone.
272 The C-support is mounted to an aluminum baseplate
273 that defines the position of the SVT with respect to the
274 vacuum chamber. Figure 5 shows a photograph of both
275 completed detector halves prior to final assembly.



276 Figure 5: Both halves of the HPS Test Run SVT after final assembly at SLAC. The cooling manifolds and integrated cable runs are clearly seen.

278 **4.2. Components**

279 The sensors for the SVT are *p*-on-*n*, single sided,
 280 AC coupled, polysilicon-biased microstrip sensors fab-
 281 ricated on < 100 > silicon and have 30 (60) μm sense
 282 (readout) pitch over their $4 \times 10 \text{ cm}^2$ surface. This sen-
 283 sor technology was selected to match the requirement
 284 of a $< 1\% X_0$ per layer, single-hit resolution better than
 285 $50 \mu\text{m}$ and tolerant of a radiation dose of approximately
 286 $1.5 \times 10^{14} 1 \text{ MeV}$ neutron equivalent/ cm^2 for a six month
 287 run. The sensors were purchased from the Hamamatsu
 288 Photonics Corporation for the cancelled Run 2b upgrade
 289 of the DØ experiment [9] which satisfied the require-
 290 ment that the technology must be mature and available
 291 within the time and budget constraints.

292 Despite having only small spots with very high occu-
 293 pancy (up to 4 MHz/mm^2) closest to the primary beam,
 294 the rates are still high and lowering the peak occupancy
 295 to approximately 1% for tracking requires a trigger win-
 296 dows and hit time tagging of roughly 8 ns. The ECal
 297 readout and trigger described in Sec. 5.3 can achieve
 298 such resolution. To reach this performance the sen-
 299 sors for the SVT are readout by the APV25 ASIC de-
 300 veloped for the CMS experiment at CERN [10]. The
 301 APV25 can capture successive samples of the shaper
 302 output in groups of three at a sampling rate of approx-
 303 imately 40 MHz. By fitting the known *CR-RC* shaping
 304 curve to these samples, the initial time of the hit can
 305 be determined to a precision of 2 ns for $S/N \approx 25$ [11].
 306 For electron beam running, six-sample readout and the
 307 shortest possible shaping time (35 ns) is used to best
 308 distinguish hits that overlap in time. The APV25 ASICs
 309 are hosted on simple FR4 hybrid readout boards, out-
 310 side the tracking volume, with a short twisted-pair pig-
 311 tail cable to provide power and configuration and signal
 312 readout. Along with a single sensor, these are glued
 313 to a polyamide-laminated carbon fiber composite back-
 314 ing making up a half-module. A window is machined
 315 in the carbon fiber leaving only a frame around the pe-
 316 riphery of the silicon to minimize material. A $50 \mu\text{m}$
 317 sheet of polyamide is laminated to the surface of the
 318 carbon fiber with 1 mm overhang at all openings to en-
 319 sure good isolation between the backside of the sensor,
 320 carrying high-voltage bias, and the carbon fiber which
 321 is held near ground.

322 The sensor modules for the SVT consist of a pair
 323 of identical half-modules, sandwiched back-to-back
 324 around an aluminum cooling block at one end and a sim-
 325 ilar PEEK spacer block at the other. Figure 6 shows a
 326 single module after assembly. The cooling block pro-
 327 vides the primary mechanical support for the module as
 328 well as cooling via copper tubes pressed into grooves

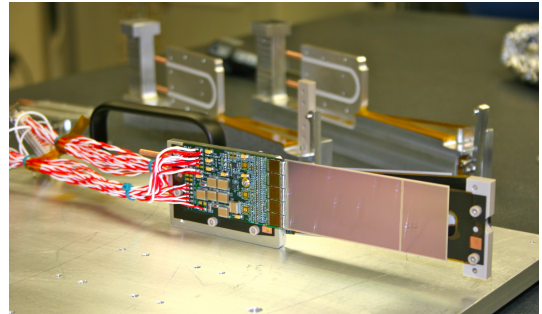


Figure 6: A prototype module assembly (foreground) with the 50 mrad (left) and 100 mrad (right) module assembly fixtures in the background. A pair of cooling blocks and a spacer block can be seen on the fixtures.

in the plates. The spacer block defines the spacing between the sensors at the far end of the module, stiffens the module structure, and improves the stability of the sensor alignment. The average support material in the tracking volume is approximately $0.06\% X_0$ per double-sided module for a total material budget of 0.7% per layer.

The total SVT power consumption budget of about 50 W is removed by a water/glycol mixture circulated through a flexible manifold attached to the copper tubes in the cooling blocks. During the Test run the sensors where operated at around 23°C . The power consumption is dominated by five APV25 ASICs on each hybrid board consuming approximately 2 W, radiant heat load is less than 0.5 W per sensor and leakage current is only significant in a small spot after irradiation.

345 **4.3. Production, Assembly and Shipping**

346 Hybrids with APV25 ASICs underwent quick qualifi-
 347 cation testing and each half-module was run at low tem-
 348 perature ($\approx 5^\circ\text{C}$) and fully characterized for pedestals,
 349 gains, noise and time response after assembly. Of 29
 350 half-modules built, 28 passed qualification testing, leav-
 351 ing 8 spare modules after completion of the SVT, all ca-
 352 pable of 1000 V bias voltage without breakdown. Full-
 353 module assembly and mechanical surveys were per-
 354 formed at SLAC before final assembly, testing and ship-
 355 ping of the SVT to JLab. A custom shipping container
 356 with nested crates and redundant isolation for shock and
 357 vibration was built in order to safely send the partly as-
 358 sembled SVT to JLab. At JLab, the entire SVT was
 359 integrated with the full DAQ and the power supplies be-
 360 fore moving the module-loaded support plates to Hall B
 361 for final mechanical assembly and installation inside of
 362 the vacuum chamber.

363 **4.4. Alignment**

364 The SVT was aligned using a combination of optical,
 365 laser and touch probe surveys at SLAC and JLab. The
 366 optical survey of individual modules with precision of
 367 a few μm are combined with a touch-probe survey of
 368 the overall SVT support structure, with 25-100 μm pre-
 369 cision, to locate the silicon sensor layers with respect
 370 to the support plates and the mechanical survey balls
 371 on the base plate. After full assembly and installation
 372 of the SVT at JLab, a mechanical survey of the SVT
 373 base plate position inside the pair spectrometer vacuum
 374 chamber is used to determine the global position of the
 375 SVT with respect to CEBAF beam line. The resulting
 376 survey-based alignment has the position of the silicon
 377 sensors correct to within a few hundred microns mea-
 378 sured from tracks in the HPS Test Run data. A more
 379 sophisticated global track-based alignment technique to
 380 reach final alignment precision well below 50 μm is be-
 381 ing developed.

382 **5. Electromagnetic Calorimeter**

383 The electromagnetic calorimeter (ECal), installed
 384 downstream of the PS dipole magnet, performs two es-
 385 sential functions for the experiment: it provides a trigger
 386 signal to select what events to read out from the detector
 387 sub-systems and is used in the analysis to identify elec-
 388 trons and positrons. The technology and design choices
 389 are largely driven by the need for a compact forward de-
 390 sign covering the SVT A' acceptance and able to fully
 391 absorb electrons and positrons with energy between 0.5-
 392 6.5 GeV, fine granularity and signal readout speed to
 393 handle 1 MHz/cm² of electromagnetic background and
 394 be radiation hard. The PbWO₄ crystal inner calorime-
 395 ter of the CLAS detector [12], in operation since 2005
 396 in Hall B, meets all the requirements set by HPS. The
 397 modules from this calorimeter have been subsequently
 398 repurposed for HPS.

399 **5.1. Components**

400 The ECal module shown in Fig. 7 is based on a
 401 tapered 160 mm long PbWO₄ crystal with a 13.3 \times
 402 13.3 mm² (16 \times 16 mm²) front (rear) face wrapped in
 403 VM2000 multilayer polymer mirror film. The scintilla-
 404 tion light, approximately 3 photoelectrons/MeV, is read-
 405 out by a 5 \times 5 mm² Hamamatsu S8664-55 Avalanche
 406 Photodiode (APD) with 75% quantum efficiency glued
 407 to the rear face surface using MeltMount 1.7 thermal
 408 plastic adhesive. The low gain of APDs (~ 200) was
 409 compensated with custom made preamplifier boards,
 410 which provide a factor of 2333 amplification of the APD
 411 signal.

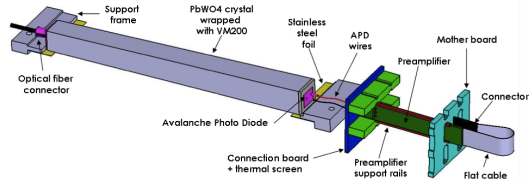


Figure 7: Schematic view of an ECal module.

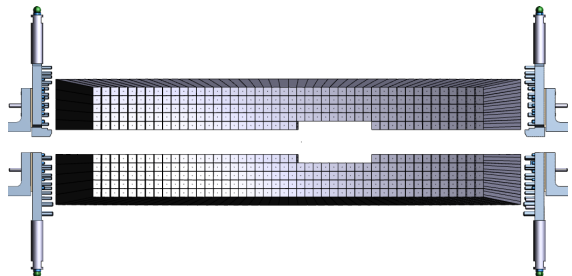


Figure 8: Rendered layout view of the ECal looking downstream.

412 **5.2. Layout**

413 Similar to the SVT, the ECal is built in two separate
 414 halves that are mirror reflections of one another about
 415 the plane of the nominal electron beam to avoid interfer-
 416 ing with the 15 mrad "dead zone". As shown in Fig. 8,
 417 the 221 modules in each half, supported by aluminum
 418 support frames, are arranged in rectangular formation
 419 with 5 layers and 46 crystals/layer except for the layer
 420 closest to the beam where 9 modules were removed to
 421 allow a larger opening for the outgoing electron and
 422 photon beams. Each half was enclosed in a tempera-
 423 ture controlled box (< 1° F stability and < 4° F unifor-
 424 mity) to stabilize the crystal light yield and the opera-
 425 tion of the APDs and its preamplifiers. Four printed circuit
 426 boards mounted on the backplane penetrated the enclo-
 427 sure and was used to supply the ± 5 V operating voltage
 428 for the preamplifiers, 400 V bias voltage to the APDs,
 429 and to read out signals from the APDs. Each half of
 430 the ECal was divided into 12 bias voltage groups with a
 431 gain uniformity of about 20%.

432 During the HPS Test Run, both halves were held in
 433 place by four vertical bars attached to an above rail,
 434 placing the front face of the crystals 147 cm from the
 435 upstream edge of the magnet and with a 8.7 cm gap
 436 between the innermost edge of the crystals in the two
 437 halves.

438 **5.3. Signal readout**

439 After a 2:1 signal splitter, 1/3 of an amplified APD
 440 signal was fed to a single channel of a JLab flash ADC
 441 (FADC) board [13]. 2/3 of the signal was sent to a
 442 discriminator module and then to a TDC for a timing
 443 measurement. The FADC boards are high speed VXS
 444 modules digitizing up to 16 APD signals at 250 MHz
 445 and storing samples in 8 μ s deep pipelines with 12-bit
 446 resolution. When a trigger is received, the part of the
 447 pipeline from 5 samples before and 30 after the sig-
 448 nals crossed a programmable threshold (for the HPS Test
 449 Run this was set to ≈ 70 MeV) are summed and stored
 450 in a 17-bit register for readout. In addition a 4 ns res-
 451 olution timestamp of the threshold crossing is reported
 452 in the readout for each pulse. This scheme significantly
 453 compresses the data output of the FADC. During offline
 454 data analysis, a calibrated pedestal value is subtracted
 455 to obtain the actual summed energy. Two 20-slot VXS
 456 crates with 14 (13) FADC boards were employed in the
 457 HPS Test Run to read out the top (bottom) half of the
 458 ECal. In the HPS Test Run 385 out of 442 modules
 459 (87%) were used in offline reconstruction, 39 modules
 460 were disabled or not read out (no FADC channel avail-
 461 able, no APD bias voltage or masked out due to exces-
 462 sive noise) and 18 were masked offline due to noise.

463 **6. Trigger and Data Acquisition**

464 The DAQ system handles acquisition of data from the
 465 ECal and SVT sub-detectors with two DAQ architec-
 466 tures. The SVT DAQ is based on Advanced Telecom
 467 Communications Architecture (ATCA) hardware while
 468 the ECal uses VMEbus Switched Serial (VXS) based
 469 hardware. Data from the sub-detectors are only readout
 470 when a trigger signal from the trigger system is received
 471 formed on input from the ECal.

472 **6.1. Trigger system**

473 The trigger system is designed to select time coinci-
 474 dences of electromagnetic clusters in the top and bot-
 475 tom halves of the ECal. Figure 9 shows a schematic
 476 overview of each stage of the system. Each channel on
 477 the FADC board has an independent data path to send 5-
 478 bit pulse energy and 3-bit pulse arrival time information
 479 every 32 ns to a trigger processing board (CTP), which
 480 is in the same crate. The 3-bit pulse arrival time allows
 481 the trigger to know the pulse timing at 4 ns resolution.
 482 Contrary to the readout path described in Sec. 5.3, this
 483 energy is a pedestal subtracted time-over-threshold sum
 484 with programmable offsets and minimum threshold dis-
 485 criminator for each channel. With input from all FADC

486 channels, i.e. one half of the ECal, the CTP performs
 487 cluster finding and calculates cluster energy and tim-
 488 ing information. The 3x3 fixed-window, highly parallel,
 489 FPGA-based cluster algorithm simultaneously searches
 490 for up to 125 clusters with energy sum larger than the
 491 programmable energy threshold (≈ 270 MeV). Crystals
 492 in the fixed-window are included in the sum if the lead-
 493 ing edge of the pulse occurred within a 32 ns time win-
 494 dow to take into account clock skew and jitter through-
 495 out the system. The CTP only accepts clusters with the
 496 highest energy 3x3 window locally to deal with over-
 497 lapping and very large clusters. The sub-system board
 498 (SSP) receives the clusters from the top and bottom half
 499 CTP at a maximum of 250MHz and searches for pairs
 500 of clusters in a 8 ns wide coincidence window. The SSP
 501 sends triggers to the trigger supervisor (TS), which gen-
 502 erates all the necessary signals and controls the entire
 503 DAQ system readout through the trigger interface units
 504 installed in every crate that participate in the readout
 505 process.

506 The trigger system is free-running and driven by the
 507 250 MHz global clock and has essentially zero dead
 508 time at the occupancies expected for HPS. The trigger
 509 supervisor can apply dead time if necessary, for exam-
 510 ple on a ‘busy’ or ‘full’ condition from the front-end
 511 electronics. The system is designed to handle trigger
 512 rates above 50 kHz and has a latency set to ≈ 3 μ s to
 513 match that required by the SVT APV25 ASIC. During
 514 the HPS Test Run, for the most part the trigger system
 515 required only a single cluster in either the top or bot-
 516 tom Ecal halves and was tested to trigger rates above
 517 100 kHz by lowering thresholds.

518 **6.2. SVT Data Acquisition**

519 The SVT DAQ is based on the Reconfigurable Clus-
 520 ter Element (RCE) and cluster interconnect concept de-
 521 veloped at SLAC as generic building blocks for DAQ
 522 systems. The RCE is a generic computational build-
 523 ing block, housed on a separate daughter card called

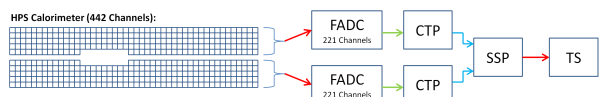


Figure 9: Block diagram of the ECAL trigger system consisting of the FADC that samples and digitizes signals for each detector channel and sends them for cluster finding in the CTP. The CTP clusters are sent to the SSP where the final trigger decision is taken based on pairs of clusters in both halves of the ECal. The decision is sent to the Trigger Supervisor (TS) that generates the necessary signals to readout the sub-detectors.



Figure 10: The SVT DAQ COB board with four data processing daughter cards (DPMs) visible on the left side.

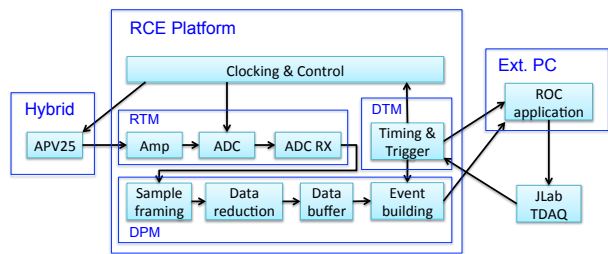


Figure 11: Block diagram overview of the SVT DAQ.

524 Data Processing Module (DPM), that are realized on an
 525 ATCA front board called the Cluster On Board (COB),
 526 see Fig. 10. The first generation RCE used in the HPS
 527 Test Run consisted of a Virtex 5 FPGA with 1 GB
 528 of DDR3 RAM. A schematic overview of the system
 529 is shown in Fig. 11. The analog outputs of up to 12
 530 SVT half-modules (60 APV25 ASICs) are digitized on
 531 the Rear-Transition-Module (RTM), a custom board on
 532 the back side of the ATCA crate, interfacing the HPS-
 533 specific readout to the generic DAQ components on the
 534 COB. A pre-amplifier converts the APV25 differential
 535 current output to a different voltage output scaled to the
 536 sensitive range of a 14-bit ADC operating at the system
 537 clock of 41.667 MHz. The RTM is organized into four
 538 sections with each section supporting three SVT half-
 539 module hybrids (15 APV25 ASICs). The RTM also in-
 540 cludes a 4-channel fiber optic module and supporting
 541 logic which is used to interface to the JLab trigger sys-
 542 tem supervisor. Each section of the RTM is input to a
 543 DPM which apply thresholds for data reduction and or-
 544 ganizes the sample data into UDP datagrams. The DPM
 545 also hosts an I²C controller used to configure and mon-
 546 itor the APV25 ASICs. A single ATCA crate with two
 547 COB cards was used, one supporting four DPMs and
 548 one supporting 3 DPMs and one DPM that is config-
 549 ured as the trigger and data transmission module. The

550 two COB cards and their DPMs are interconnected with
 551 a 10 Gb/s switch card [14] which also hosts two 1Gb/s
 552 Ethernet interfaces to the external SVT DAQ PC.

553 The external PC supports three network interfaces;
 554 two standard 1 Gb/s Ethernet and one custom low la-
 555 tency data reception card. The first is used for slow con-
 556 trol and monitoring of the 8 DPM modules and the sec-
 557 ond serves as the interface to the JLAB data acquisition
 558 system. The third custom low latency network interface
 559 is used to receive data from the ATCA crate and sup-
 560 ports a low latency, reliable TTL trigger acknowledge
 561 interface to the trigger DPM. This PC hosts the SVT
 562 control and monitoring software as well as the Read Out
 563 Controller application used to interface with the JLab
 564 DAQ.

565 In order to minimize cable length for the analog
 566 APV25 output signal the ATCA crate was located ap-
 567 proximately 1 m from the beam line, next to our ca-
 568 ble vacuum feed-troughs. Before shielding with lead-
 569 blankets was arranged, we observed two failures of
 570 normally reliable ATCA crate power supplies, time-
 571 correlated to beam instabilities.

572 While trigger rates during the HPS Test Run was sig-
 573 nificantly lower this system was tested at trigger rates
 574 up to 20 kHz and 50 MB/s.

6.3. General Data Acquisition and Online Computing

576 Every crate participating in the readout process con-
 577 tains a Readout Controller (ROC) that collects digitized
 578 information, processes it, and sends it on to the event
 579 builder. For the ECal, both VXS crates run ROC ap-
 580 plications in a single blade Intel-based CPU module run-
 581 ning CentOS Linux OS. For the SVT DAQ, the ROC
 582 application runs on the external PC under RHEL. The
 583 event builder assembles information from the ROCs into
 584 a single event which is passed to the event recorder that
 585 writes it to a RAID5-based data storage system capa-
 586 ble of handling up to 100 MB/s. The event builder and
 587 other critical components run on multicore Intel-based
 588 multi-CPU servers. The DAQ network system is a net-
 589 work router providing 10 Gb/s high-speed connection to
 590 the JLab computing facility for long-term storage. For
 591 the HPS Test Run, both the SVT and ECal ROC had a
 592 1 Gb/s link to the network router.

7. Reconstruction and Performance

7.1. SVT Performance

593 For the duration of the HPS Test Run all SVT mod-
 594 ules and APV25 chips were configured to their nominal
 595 operating points [15] with all sensors reverse-biased at

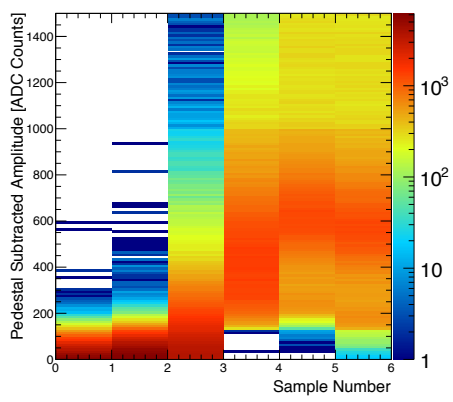


Figure 12: Accumulation of six pedestal-subtracted samples from individual SVT channels associated with hits on tracks.

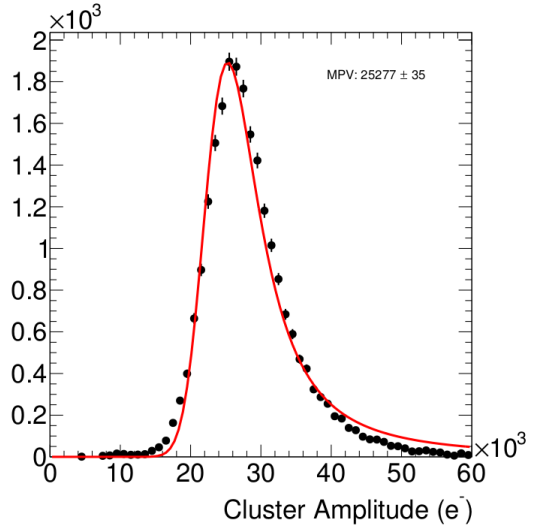


Figure 13: The cluster charge distribution for hits associated with track follow the characteristic Landau shape.

598 180 V. The sensors were operated within a temperature
 599 range of 20 – 24°C. Approximately 97% of the 12,780
 600 SVT channels were found to be operating normally; the
 601 fraction of dead or noisy channels varied from 2.4%
 602 to 4.7% throughout the HPS Test Run. Most of these
 603 losses were due to 2-4 misconfigured APV25 ASICs, a
 604 known noisy half-module and problems in two particu-
 605 lar APV25 ASICs.

606 7.1.1. Cluster and Hit Reconstruction

607 After a trigger is received, the amplitude of every
 608 APV25 analogue output is sampled and digitized in
 609 six consecutive time bins, separated by roughly 25 ns.
 610 The typical, pedestal subtracted, pulse shape obtained
 611 is shown in Fig. 12. As the figure demonstrates, the
 612 SVT was well timed-in to the trigger with the rise of the
 613 pulse at the 3rd sampling point. In order to find the time,
 614 t_0 , and amplitude of each hit, the six samples from each
 615 channel are fitted to an ideal $CR - RC$ function. Note that
 616 in the HPS Test Run the APV25 ASICs were operating
 617 with a 50 ns shaping time. These hits are passed through
 618 a simple clustering algorithm which forms clusters by
 619 grouping adjacent strips with the position of a cluster on
 620 the sensor determined by the amplitude-weighted mean.
 621 With a linear gain up to ≈ 3 MIPs, the cluster charge
 622 for hits associated with a track follow the characteristic
 623 Landau shape. A noise level between $1.1 - 1.5 \times 10^3$
 624 electrons was established through multiple calibration
 625 runs giving a signal to noise ratio of 21 – 25. Lab-
 626 based radioactive source tests was used to provide the
 627 absolute charge normalization. After clustering hits on
 628 a sensor, the hit time for each cluster is computed as
 629 the amplitude-weighted average of the individually fit-

630 ted t_0 on each channel. The t_0 resolution is studied by
 631 comparing the cluster hit time with the average of all
 632 cluster hit times on the track shown in Fig. 14. After
 633 correcting for offsets from each sensor (time-of-flight
 634 and clock phase) and accounting for the correlation be-
 635 tween the t_0 and track time, the extracted t_0 resolution is
 636 2.6 ns. This is somewhat worse than the approximately
 637 2 ns resolution expected for S/N 25 which we attribute
 638 to the true pulse shape differing from our idealized fit
 639 function which will be improved in the future. Reduc-
 640 ing the APV25 ASIC pulse shaping time to 35 ns will
 641 also improve time resolution. These results show that
 642 we can operate with the six sample readout mode of the
 643 APV25 chip and achieve time resolution adequate for
 644 pileup rejection during electron running in HPS.

645 Good agreement between observed and simulated oc-
 646 cupancies after taking into account dead or noisy chan-
 647 nels. The hit reconstruction efficiency was estimated by
 648 measuring the number of good tracks with a hit close to
 649 the extrapolated intersection of a given sensor that was
 650 excluded from the track fit itself. Tracks which inter-
 651 sect regions with known bad channels or very close to
 652 in the edge region are excluded. The hit reconstruction
 653 efficiency, see Fig. 15, was measured to be above 98%
 654 and fairly uniform across the SVT.

655 The spatial resolution of similar microstrip sensors is
 656 well established by test beam data, against which the
 657 charge deposition model in the simulation is validated.
 658 This resolution can be parameterized as a function of the
 659 total signal to single-strip noise and the crossing angle

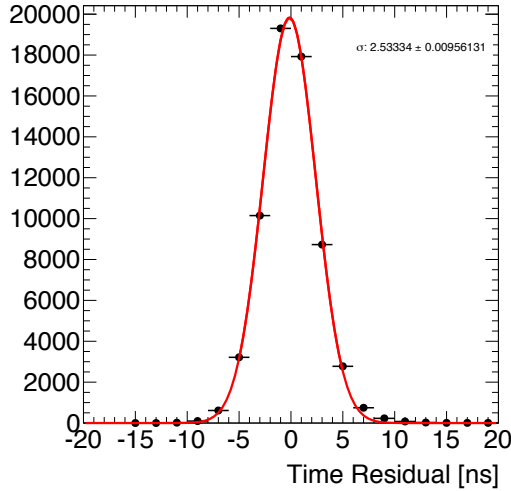


Figure 14: The residual of individual cluster times with the average of all clusters on the track.

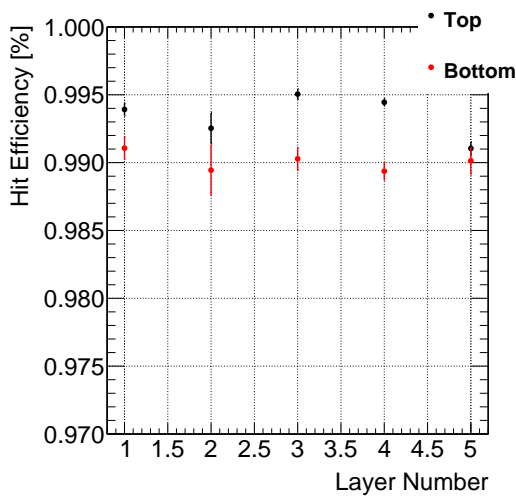


Figure 15: The hit reconstruction efficiency as a function of detector layer.

of tracks through the sensor. The single-hit resolution for charged particles with signal to noise ratio above 20, as demonstrated here, is relatively constant at approximately 6 μm for tracks that enter approximately normal to the sensors as in HPS.

7.1.2. Momentum and Vertexing Resolution

By selecting e^+e^- pairs from the triggered events we are able to study basic distributions of pair production kinematics. Pairs of oppositely charged tracks, one in the top and one in the bottom half of the SVT, with momentum larger than 400 MeV were selected. The pair production kinematics are relatively well reproduced as shown in Fig. 16.

The expected momentum resolution from simulation is between 4-5% for tracks in the momentum range of the HPS Test Run. By comparing the shapes of the kinematic distributions for single- and two track events between data and simulation we estimate an agreement with the nominal scale and resolution to within 10%.

In the HPS Test Run, as well as in electron running with HPS, the dominant source of uncertainty in the tracking and vertexing is multiple Coulomb scattering. For the vertexing performance the foremost difference compared to electron beam running is that the target was located approximately 67 cm upstream from our nominal target position; giving almost collinear tracks in the detector. The increased lever arm over which tracks are extrapolated widens the resolution with up to a factor of eight (depending on momentum) compared to what is achieved at the nominal electron target position for HPS. Figure 17 shows the horizontal and vertical positions of the extrapolated track at the converter position. While residual alignment show small shifts, the good agreement between data and simulated events of the widths indicates a good understanding of the material budget and distribution in the SVT. Having the dominant contribution to the vertex resolution approximately right demonstrates that the resolution in HPS, with a target at 10 cm, will be as calculated.

7.2. ECal Performance

The integrated pulse of each FADC channel was converted to energy by subtracting a pedestal and applying a conversion factor to convert ADC counts to energy. The pedestals are measured using special runs where each trigger records 100 samples of signals from the APDs with 4 ns between each sample. The pedestals were extracted from the part of the window before the

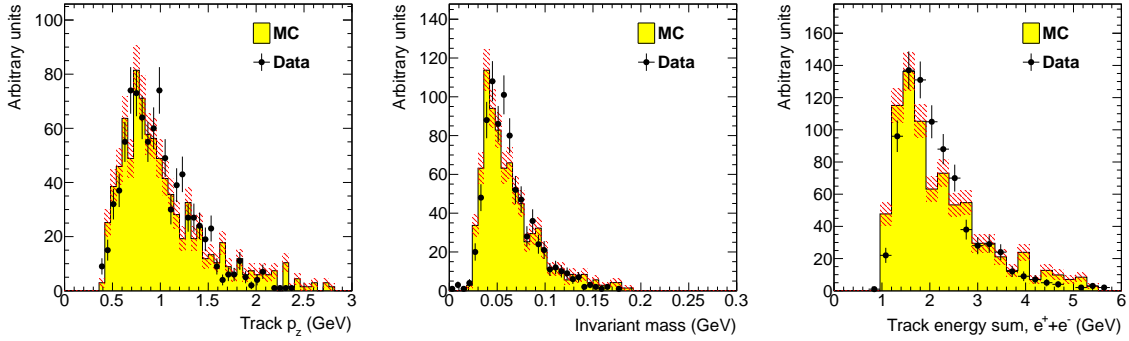


Figure 16: Kinematic distributions for e^+e^- pairs selected by opposite charged tracks in the top and bottom half of the tracker: track momentum in the top half of the SVT (left), invariant mass (middle) and the sum of the track momentum for the pair (right).

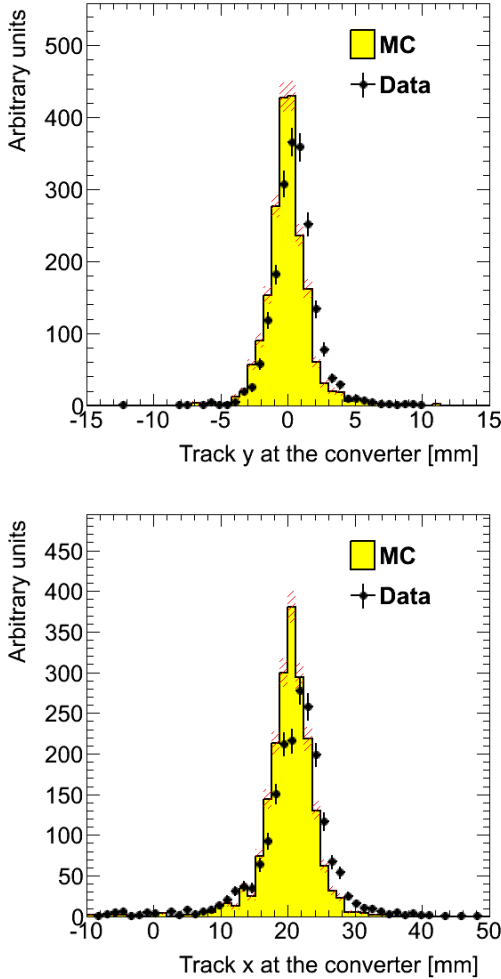


Figure 17: Vertical (top) and horizontal (bottom) extrapolated track position at the converter position taking into account the measured fringe field.

708 actual hit in the calorimeter. Modules with signal above
 709 the threshold are clustered using a simple algorithm
 710 similar to the one deployed for the trigger (see Sec. 6.1).
 711 Due to the high effective readout threshold of 73 MeV
 712 the average number of crystals in a cluster was ~ 3 and
 713 the simple clustering algorithm worked well for recon-
 714 struction of the detected shower energy. An average
 715 noise level of approximately 15 MeV was measured in
 716 special pedestal runs.

717 The ratio of the ECal cluster energy E to the momen-
 718 tum p of a matched track in the SVT was used to de-
 719 termine the conversion factors from ADC counts to en-
 720 ergy. To compare data and simulation, all inoperable or
 721 noisy channels in the SVT and ECal were disabled in
 722 both data and simulation so that any efficiency or bias
 723 that affect the data should be reflected in the simulation.
 724 Iteratively, conversion coefficients for each crystal were
 725 adjusted until the E/p ratio in data and simulation were
 726 similar. The distribution of the E/p ratio in data and
 727 simulation are compared in Fig. 18. The peak position
 728 of the distribution indicates the sampling fraction
 729 of the ECal, the fraction of the incident particle energy
 730 measured in the cluster. The width and tails of the distri-
 731 bution in data indicates imperfect calibration and noise
 732 of the ECal modules. This level of calibration and the
 733 agreement with simulation was found to be sufficient to
 734 study normalized event rates in the HPS Test Run.

735 7.3. Trigger Performance

736 As described above in Sec. 6, the energy from each
 737 crystal is measured differently in the trigger and what
 738 is readout from the ECal. The trigger performance
 739 was studied by simulating the trigger for each event
 740 and comparing to how the events were actually trig-
 741 gered. To eliminate trigger bias, we use a tag and probe
 742 method: to study the trigger performance in one half

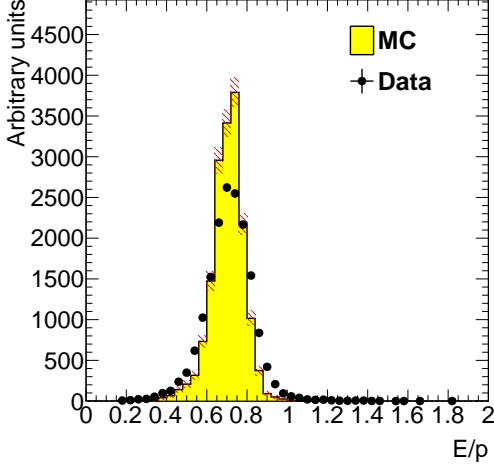


Figure 18: The ECal energy over track momentum ratio (E/p) comparing data and simulation for single cluster triggers in the top half of the ECal.

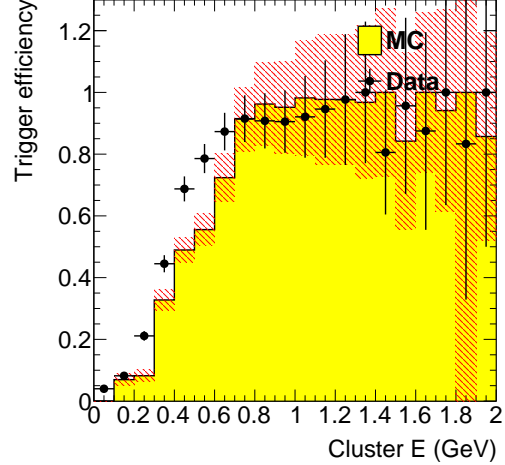


Figure 19: Trigger efficiency in both halves of the ECal for data and simulation as a function of cluster energy.

Converter (% X_0)	1.60	0.45	0.18
EGS5	1162 ± 112	255 ± 28	94 ± 17
GEANT4	2633 ± 250	371 ± 38	114 ± 18
Observed	1064 ± 2	196 ± 1	92 ± 1

Table 4: Observed and predicted event rate (in Hz) normalized to 90 nA for three different converter thicknesses. The uncertainty on the prediction includes systematic uncertainties from ECal alignment, background normalization, beam current normalization and limited statistics in the simulation.

of the ECal, we select events which triggered the other half and where there was exactly one probe cluster in the ECal half under study. We then measure trigger efficiency as the fraction of tagged events that fired the trigger in the probe half as a function of the probe cluster energy, shown in Fig. 19. The trigger turn-on is slow and reaches an uneven plateau just below 1 GeV for two reasons; gain variations between different crystals lead to the threshold variations and the nonlinearity of the time-over-threshold integral means that the effective threshold is higher for clusters that span multiple crystals. The effective trigger threshold is therefore dependent on position and energy of the particle as well as cluster multiplicity.

As a cross-check we simulate the FADC trigger path by converting from readout hits (with fixed-size window integration) to trigger hits (time-over-threshold integration). The CTP clustering algorithm and the trigger decision from the SSP is simulated before we compare the trigger decision and trigger time to what was reported by the actual trigger. For every event, the trigger reports the trigger decision as a bit mask (top half, bottom half or both) and the time the trigger fired. The turn-on from the trigger threshold was measured to be 1280 in units of ADC counts as expected. The threshold was not perfectly sharp because of uncertainties in the conversion from readout to trigger hits described above, but based on comparisons with simulation we found that the trigger worked exactly as specified.

7.4. Trigger Rate Comparisons

Trigger rates observed in the HPS Test Run are dominated by multiple Coulomb scattered e^+e^- pairs in the converter. In simulated events, the rate of triggers depend on the modeling of the pairs angular distribution and the subsequent multiple Coulomb scattering in the converter. Rates from different converter thicknesses are used to study the varying multiple Coulomb scattering contribution (pair production angle is constant). Restricting clusters to a well calibrated region of the ECal and subtracting the "no converter" background we see agreement with the rates predicted by the EGS5 simulation program, see Tab. 7.4. This gives further confidence that the dominant source of background occupancy for HPS, multiple Coulomb scattered beam electrons, is well described [16, 17, 18].

8. Summary and Outlook

The HPS Test Run experiment, using a simplified version of the apparatus planned for the full HPS ex-

periment in a parasitic photon beam, demonstrated the feasibility of the detector technologies proposed for the silicon vertex tracker, electromagnetic calorimeter, and data acquisition systems. Performance from each of these subsystems has been shown to be adequate to conduct the full experiment successfully. Studies of multiple Coulomb scattering tails of electrons and positrons from photon conversions further backs expectations from simulation, giving credence to estimates of the detector backgrounds expected in electron beam running for HPS.

9. Acknowledgements

The authors are grateful for the support from Hall B at JLab and especially the Hall B engineering group for support during installation and decommissioning. They also would like to commend the CEBAF personnel for good beam performance; the last few hours of operating CEBAF6. The tremendous support from home institutions and supporting staff also needs praise from the authors.

This work has been supported by the US Department of Energy.

References

- [1] B. Holdom, Two U(1)'s and Epsilon Charge Shifts, Phys.Lett. B166 (1986) 196.
- [2] R. Essig, J. A. Jaros, W. Wester, P. H. Adrian, S. Andreas, et al., Dark Sectors and New, Light, Weakly-Coupled Particles (2013).
- [3] M. Pospelov, Secluded U(1) below the weak scale, Phys.Rev. D80 (2009) 095002.
- [4] N. Arkani-Hamed, D. P. Finkbeiner, T. R. Slatyer, N. Weiner, A Theory of Dark Matter, Phys.Rev. D79 (2009) 015014.
- [5] J. D. Bjorken, R. Essig, P. Schuster, N. Toro, New Fixed-Target Experiments to Search for Dark Gauge Forces, Phys.Rev. D80 (2009) 075018.
- [6] A. G. *et al.* (HPS Collaboration), HPS Heavy Photon Search Proposal, 2010.
- [7] A. Sandorfi, *et al.*, 2012. URL: http://www.jlab.org/exp_prog/proposals/06/PR-06-101.pdf.
- [8] I. Rashevskaya, S. Bettarini, G. Rizzo, L. Bosisio, S. Dittongo, et al., Radiation damage of silicon structures with electrons of 900-MeV, Nucl.Instrum.Meth. A485 (2002) 126–132.
- [9] D. S. Denisov, S. Soldner-Rembold, D0 Run IIB Silicon Detector Upgrade: Technical Design Report (2001).
- [10] M. French, L. Jones, Q. Morrissey, A. Neviani, R. Turchetta, et al., Design and results from the APV25, a deep sub-micron CMOS front-end chip for the CMS tracker, Nucl.Instrum.Meth. A466 (2001) 359–365.
- [11] M. Friedl, C. Irmler, M. Pernicka, Readout of silicon strip detectors with position and timing information, Nucl.Instrum.Meth. A598 (2009) 82–83.
- [12] A. Radyushkin, P. Stoler (Eds.), Inner Calorimeter in Clas/dvcs Experiment, 2008.
- [13] D. H., *et al.*, Integrated tests of a high speed VXS switch card and 250 MSPS flash ADCs, 2007. doi:10.1109/NSSMIC.2007.4436457.
- [14] R. Larsen, Emerging New Electronics Standards for Physics, Conf.Proc. C110904 (2011) 1981–1985.
- [15] L. Jones, APV25-S1: User guide version 2.2, RAL Microelectronics Design Group, 2011.
- [16] D. Attwood, P. Bell, S. Bull, T. McMahon, J. Wilson, et al., The scattering of muons in low Z materials, Nucl.Instrum.Meth. B251 (2006) 41–55.
- [17] G. Shen, C. Ankenbrandt, M. Atac, R. M. Brown, S. Ecklund, et al., Measurement of Multiple Scattering at 50-GeV/c to 200-GeV/c, Phys.Rev. D20 (1979) 1584.
- [18] B. Gottschalk, A. Koehler, R. Schneider, J. Sisterson, M. Wagner, Multiple coulomb scattering of 160 mev protons, Nuclear Instruments and Methods in Physics Research Section B: Beam Interactions with Materials and Atoms 74 (1993) 467 – 490.